ADVANCED ENERGY MATERIALS
www.advenergymat.de

Structure and Performance Evolution of Perovskite Solar Cells under Extreme Temperatures

Guixiang Li, Zhenhuang Su, Meng Li, Harrison Ka Hin Lee, Ram Datt, Declan Hughes, Chenyue Wang, Marion Flatken, Hans Köbler, José Juan Jerónimo-Rendon, Rajarshi Roy, Feng Yang, Jorge Pascual, Zhe Li, Wing Chung Tsoi,* Xingyu Gao, Zhaokui Wang, Michael Saliba, and Antonio Abate**

Metal halide perovskite solar cells may work for application in extreme temperatures, such as those experienced under extraterrestrial conditions. However, device performances in extreme temperatures are poorly investigated. This work systematically explores the performance of perovskite solar cells between –160 and 150 °C. In situ grazing-incidence wide-angle X-ray scattering discloses perovskite phase transition and crystal disordering as dominant factors for the temperature-dependent device efficiency deterioration. It is shown that perovskite lattice strain and relaxation originating from extreme temperature variations are recoverable, and so are the perovskite structure and photovoltaic performances. This work provides insights into the functioning under extreme temperatures, clarifying bottlenecks to overcome and the potential for extraterrestrial applications.

1. Introduction

Renewable energies are central in the international political discussion around the challenge of overcoming the shortage in fossil fuels and their climate impact.[1–3] According to the previous report, it is possible to achieve a 100% renewable electric supply by 2050.[4] Photovoltaic (PV) will be a big player in this renewable future. Halide perovskite solar cells (PSCs) are a promising technology for high efficiency and cost-effective PV. They achieved a power conversion efficiency (PCE) of 25.7%, thus competitive with established technologies, owning the advantage of

G. Li, M. Li
Key Lab for Special Functional Materials of Ministry of Education
National & Local Joint Engineering Research Center for High-efficiency Display and Lighting Technology
School of Materials Science and Engineering
Collaborative Innovation Center of Nano Functional Materials and Applications
Henan University
Kaifeng 475004, P. R. China
E-mail: mengli@henu.edu.cn

G. Li, M. Li, M. Flatken, H. Köbler, J. Pascual, A. Abate
Helmholtz-Zentrum Berlin für Materialien und Energie GmbH
14109 Berlin, Germany
E-mail: antonio.abate@helmholtz-berlin.de

Z. Su, C. Wang, X. Gao
Shanghai Synchrotron Radiation Facility (SSRF)
Shanghai Advanced Research Institute
Chinese Academy of Sciences
Shanghai 201204, P. R. China

M. Li, Z. Li
School of Engineering and Materials Science (SEMS)
Queen Mary University of London
London E1 4NS, UK

The ORCID identification number(s) for the author(s) of this article can be found under https://doi.org/10.1002/aenm.202202887.

DOI: 10.1002/aenm.202202887

H. K. H. Lee, R. Datt, D. Hughes, W. C. Tsoi
SPECIFIC
Department of Materials Science and Engineering
Faculty of Science and Engineering
Swansea University
Swansea SA1 8EN, UK
E-mail: w.c.tsoi@swansea.ac.uk

J. J. Jerónimo-Rendon, R. Roy, M. Saliba
Institute for Photovoltaics (*ipv*)
University of Stuttgart
70569 Stuttgart, Germany

F. Yang
Henan Key Laboratory of Photovoltaic Materials
School of Physics
Henan Normal University
Xinxiang 453007, P. R. China

J. Pascual
Institute for Chemical Research
Kyoto University
Kyoto 611-0011, Japan

Z. Wang
Institute of Functional Nano & Soft Materials (FUNSOM)
Jiangsu Key Laboratory for Carbon-Based Functional Materials & Devices
Soochow University
Suzhou 215123, P. R. China

M. Saliba
Helmholtz Young Investigator Group FRONTRUNNER
IEK5-Photovoltaics
Forschungszentrum Jülich
52425 Jülich, Germany

A. Abate
Department of Chemical
Materials and Production Engineering
University of Naples Federico II. Naples
80125 Naples, Italy

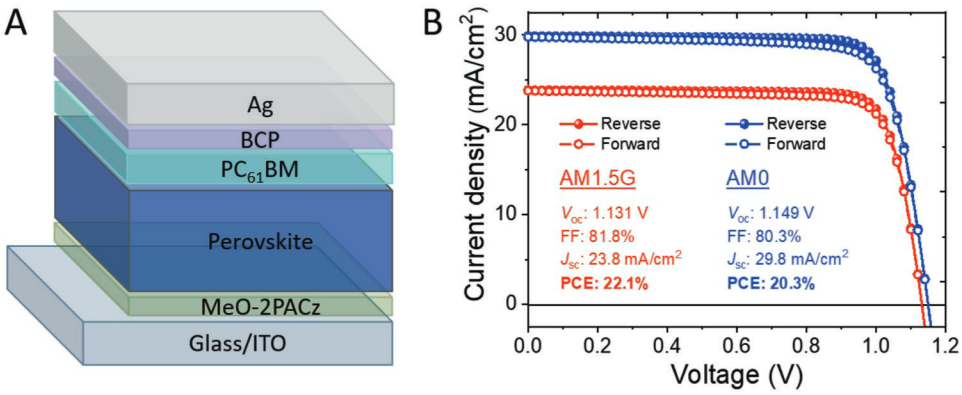

Figure 1. Power conversion efficiency under AM0 and AM1.5G. A) Device architecture. B) *J–V* curves performed under simulated AM1.5G and AM0 illumination.

processing from the solution for potential cost-effective manufacturing.[5–7] So far, the stability of PSCs remains the more significant challenge to commercialization. In addition to stability in standard environments like the earth's surface, the ability to respond to rapid and extreme temperature changes can open the way to a series of applications, including integration into aircraft for aerospace, high-altitude pseudo-satellites, international space stations, geostationary satellites, and Mars rovers.[8,9] Due to the lack of atmosphere and thus thermal transmission, the surface temperature can shift from –150 °C in the dark to 130 °C with sunlight illumination.[10,11]

Previous works investigated the temperature-dependent device PCE, focusing mainly on relatively narrow temperature windows.[11–15] For example, Shao et al. reported the p–i–n structured device PCE between room temperature and –133 °C. They indicated that the charge transport deterioration within the electron transport layers (ETL) was the leading cause of PCE losses at lower temperatures.[12] Similarly, Jena's team proposed that the hole transport layer (HTL) is responsible for PCE losses in n–i–p PSCs at high temperatures up to 120 °C.[13] Once the degradation of PSCs caused by the charge transporting layers is controlled, the intrinsic stability of the perovskite absorber is indicated as dominating in PSC operating under extreme temperatures, but it remains poorly investigated.[16] Furthermore, the extraterrestrial applications required testing the PSC's efficiency and stability in the air mass zero (AM0) solar spectrum, significantly different from the most commonly used air mass 1.5 global (AM1.5G) spectrum.[8,17] PSCs measured under AM0 solar spectrum have a record PCE of 18.8% at room temperature and unexplored stability.[18]

Herein, we investigate the performance of PSCs over a broad temperature window from –160 to 150 °C. PSCs exhibit only 6.7% PCE loss increasing the temperature to 150 °C and 27.9% PCE loss cooling to –160 °C as compared to PCEs at room temperature. Utilizing in situ grazing-incidence wide-angle X-ray scattering (GIWAXS), we directly observe the structure evolution of the perovskite, including phase transition and lattice disordering, which correlates with PCE evolution in temperature, and it is reversible over multiple temperature cycles. Our work demonstrates that PSCs are viable for application under extreme temperatures variations.

2. Results and Discussion

2.1. Photovoltaic AM0 Performance

We fabricated inverted p–i–n planar PSCs by employing a configuration of glass/ITO/MeO-2PACz/perovskite/$PC_{61}BM$/BCP/Ag to investigate the PV performances of the perovskite in temperature.[19] The corresponding device architecture is displayed in **Figure 1**A and Figure S1 (Supporting Information). The current density–voltage (*J–V*) curves with reverse and forward sweeps are evaluated under AM1.5G and AM0 solar spectra to simulate terrestrial and extraterrestrial illuminating conditions. At room temperature, solar cells show an AM1.5G PCE of 22.1% with short-circuit current density (J_{sc}) of 23.8 mA cm^{-2}, open-circuit voltage (V_{oc}) of 1.131 V and fill factor (FF) of 81.8%, see also Figure 1B. As they moved to the AM0 spectrum, PSCs reported a PCE of 20.3%, with a J_{sc} of 29.8 mA cm^{-2}, V_{oc} of 1.149 V and FF of 80.3%. The ratio of $PCE_{AM0}/PCE_{AM1.5G}$ is ≈91.8%, which is perfectly consistent with the ratio between the theoretical efficiency limit of AM0 and AM1.5G for single-junction solar cells.[9,20] The record AM0 PCE of 20.3% is detailed in Figure S2 (Supporting Information), and it is the highest ever reported.[9,18,21–23] Also, the PV parameter statistics from dozens of devices are showed Figure S3 (Supporting Information), demonstrating the performance reproducibility and reliability under AM1.5G and AM0 illumination.

2.2. Device Performance against Temperature Variation

To reveal the temperature-dependent parameters of PSCs toward extraterrestrial environments, we measured the *J–V* under AM0 illumination at different temperatures within the range of –160 to 150 °C, as shown in **Figure 2**A,B. There are the powerful mismatches on the *J–V* curves. Comparing the reverse and forward sweeps of the *J–V*, we can see that the hysteresis increases as the temperature decreases. The trend in hysteresis with temperature is represented by the hysteresis index (HI) in Figure 2C. We can observe that the hysteresis is minimal at high temperatures, but it increases rapidly as cooling down below –50 °C. Figure 2D–H displays all the device performance parameters as a function of the temperature. Going from room temperature

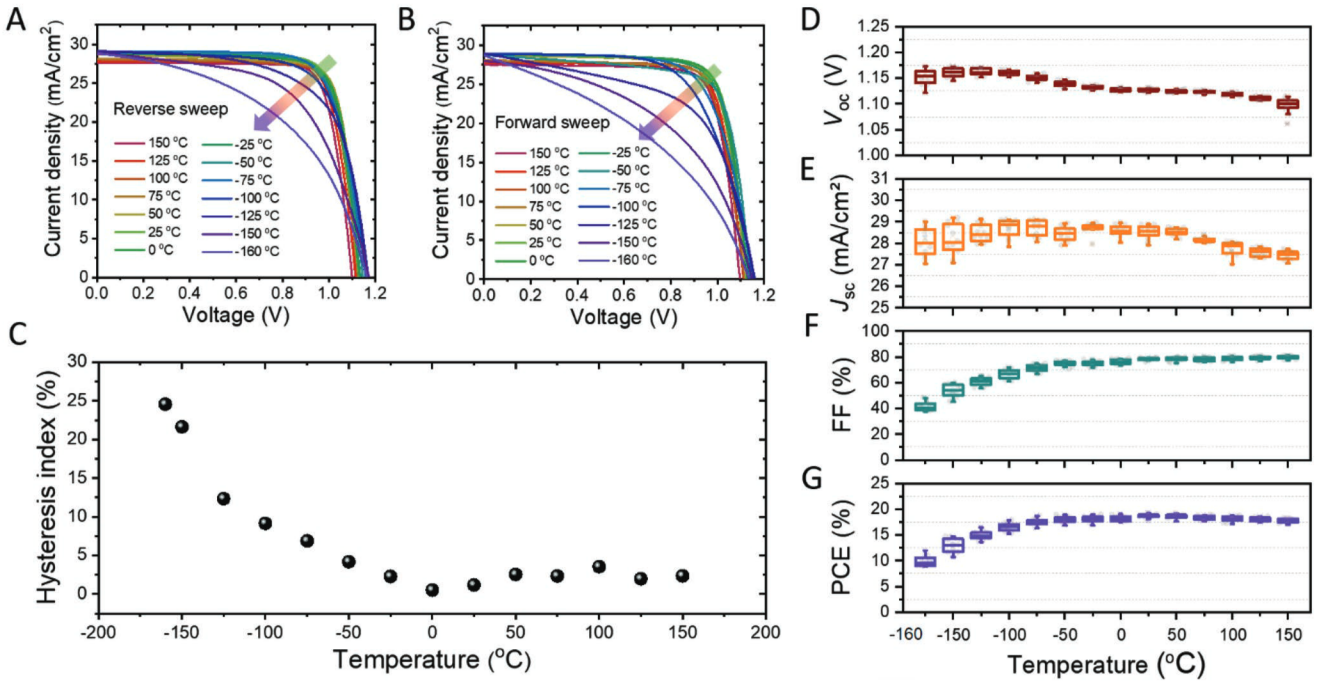

Figure 2. Device performance parameters with temperature under AM0. A) Reverse *J–V* curves, B) forward *J–V* curves, C) hysteresis index and D–G) statistical box charts of V_{oc}, J_{sc}, FF, and PCE distribution of PSCs at different temperatures.

to –160 °C, the V_{oc} increases and J_{sc} stays almost constant. At the same time, the PCE continuously decreases, in line with the substantial drop in FF. On the contrary, increasing temperature up to 150 °C, the V_{oc} decreases, leading to a gradual decline in PCE. An increase in FF alleviates the PCE degradation. The J_{sc} remains constant with fluctuation between 27.6 mA cm^{-2} at 150 °C and 28.8 mA cm^{-2} at –160 °C (Table S1, Supporting Information). The data point out that temperature-induced variation in PCE is mainly due to variations in V_{oc} and FF. We further evaluated the PSCs performance evolution under AM1.5 illumination, as shown in Figure S4, S5, and Table S2 (Supporting Information). The same trend is observed in this experiment, which supports the output of the device affected by temperature. Comparing the devices with and without the transport layers (Figure S6, Supporting Information), we found that the contribution of the perovskite layer is dominant in the performance loss.

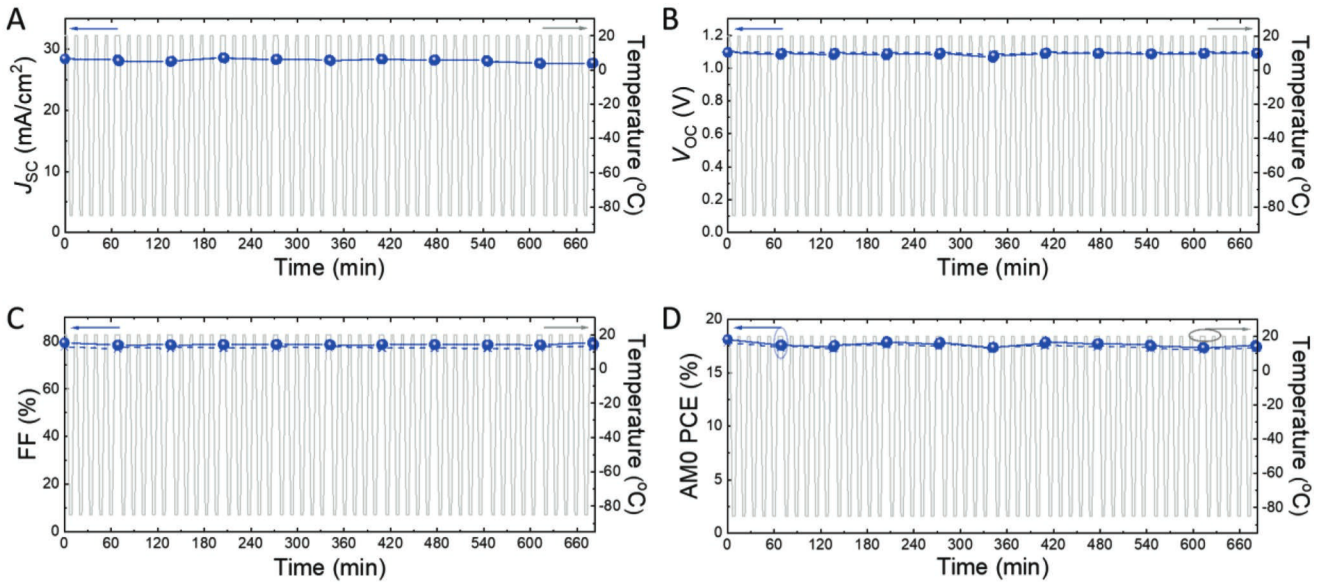

Figure 3. Device performance parameters with thermal cycling under AM0. Evolution of A) J_{sc}, B) V_{oc}, C) FF, and D) PCE of PSCs against 50 thermal cycling between 20 and –80 °C at 10 mbar under constant AM0 illumination (blue symbols correspond to the PV parameters on the left, and the solid grey lines refer to the temperature on the right).

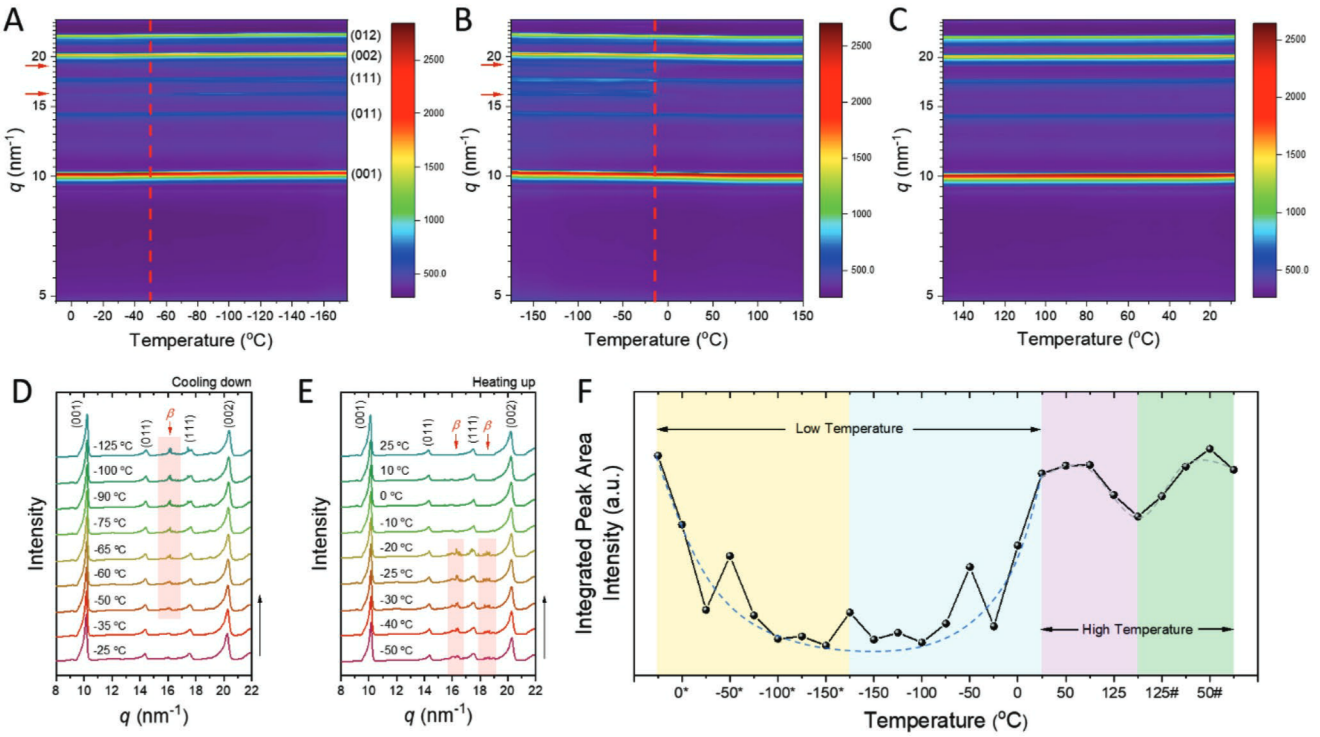

Figure 4. Phase transitions with temperature explored via in situ GIWAXS. Temperature-resolved azimuthal intensity patterns during A) cooling, B) heating, and C) cooling again to room temperature. The representative 1D plots for D) cooling and E) heating processes. F) Temperature-dependent area under the (001) diffraction peak. GIWAXS measurements were performed on perovskite films.

We performed thermal cycling (TC) measurements to explore the stability of device parameters under temperature variation from 20 to –80 °C, simulating the temperature range of high-altitude pseudo-satellites (HAPS) approaching a day's Earth's surface temperature.[9] The measurement setup is presented in Figure S7 (Supporting Information), where the device was placed in a chamber with controllable temperature and pressure. As shown in **Figure 3**, we applied 50 thermal cycles with a 30 °C min^{-1} rate to track PSCs performance. The corresponding forward and reverse sweeps results are recorded in Tables S3 and S4 (Supporting Information), respectively. Figure 3A–C illustrates that the device parameters of J_{sc}, V_{oc}, and FF are stable. After 50 thermal cycles, the device retains 97% of the original PCE (Figure 3D; Figure S8, Supporting Information). This result reflects that the device performance was basically recoverable after experiencing temperature changes. We also performed maximum power point tracking (MPPT) between –10 and 65 °C and checked the operational stability at 25, 150, and –160 °C to confirm the result in steady–state conditions (Figures S9 and S10, Supporting Information).

2.3. Temperature-Induced Perovskite Phase Conversion

To investigate the origin of PCE variation with the temperature, we performed synchrotron-based in situ GIWAXS, looking at possible changes in the crystal structure of the perovskite film.[24,25] In **Figure 4**A, the characteristic diffraction peaks at 10, 14.2, 17.5, 20, and 22.2 nm^{-1} are indexed to (001), (011), (111), (002), and (012) planes, corresponding to the cubic phase (α phase).[26,27] The perovskite is in a cubic phase at room temperature. As the temperature decreases, the diffraction peaks characteristic for the tetragonal phase (β phase) localized at q = ≈16 and ≈18.5 nm^{-1} gradually emerge.[28,29] A clear phase transition temperature can be observed ≈ –50 °C. The turning point of the phase transition is close to the temperature of a major change in device PCE (Figure 2; Figures S4 and S5, Supporting Information). Also, the tetragonal phase retains while lowering the temperature from –50 to –175 °C. Barone et al. reported that, at low temperatures, $MAPbI_3$ possessed two structural phase transitions, a tetragonal phase above –113.15 °C and the second one of orthorhombic structure below –143.15 °C.[30] However, the second orthorhombic phase transition is not observed in our GIWAXS results. The different composition of the perovskite may cause this, considering that the tri-cation CsFAMA-based perovskite has a higher temperature tolerance for conversion to orthorhombic phase than the pure MA cation-based one. While heating up again, we observe that the cubic phase replaces the tetragonal phase above –20 °C (Figure 4B). The cubic phase remains stable while heating up to 150 °C and cooling down to room temperature again, as depicted in Figure 4C. This is more clearly visible from the 1D plots in Figure 4D,E. To understand the influence of temperature variation on the device performance behind the perovskite phase transitions, we plot the integrated area under the (001) diffraction peak as a function of the temperature in Figure 4F.[31] The integrated area under the peak is positively correlated with crystallinity.[32,33] The smaller size at a temperature of ≈ –150 °C is indicative of disordering within the crystal structure. Structural disorder

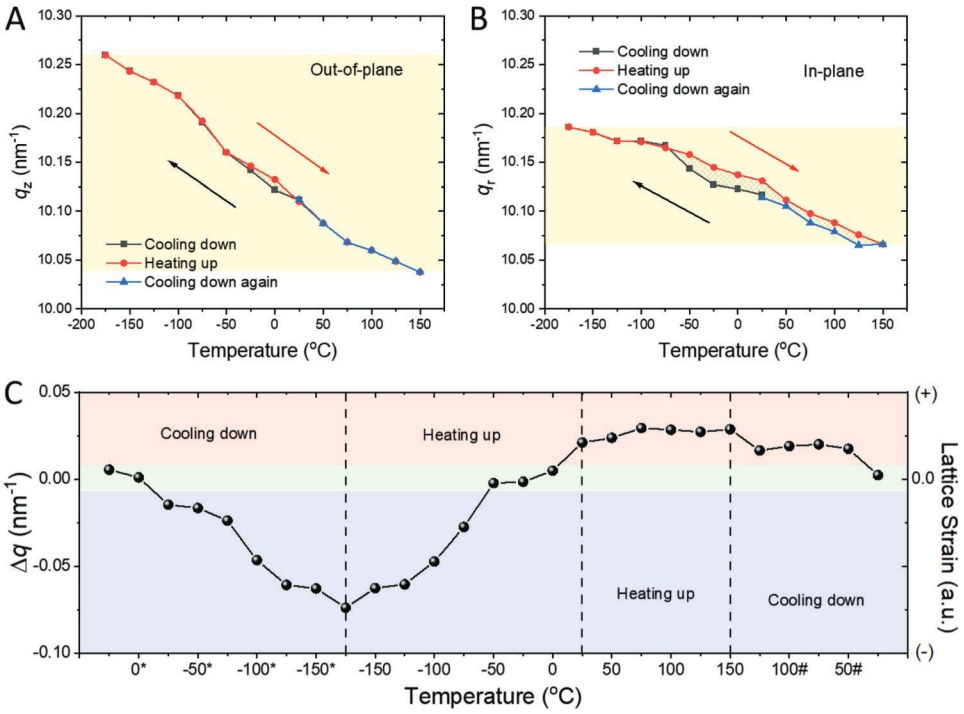

Figure 5. Strain assessment of perovskite film with temperature. The temperature-dependent evolutions of scattering vector q along A) out-of-plane direction and B) in-plane direction. C) Δq is the difference between the out-of-plane ($q_\perp$) and in-plane ($q_\parallel$) scattering vectors as a function of temperature.

results in electronic defect states, which decreases the photovoltaic performance.[34] Notably, the disorder and the photovoltaic performances recover under room temperature. Heating up to 150 °C, the impact of the disordering is significantly less severe than at a low temperature, and it remains reversible. Notice that there are the floating integrated intensities jumping between −25 and −50 °C in Figure 4F. The located temperatures are approximately coincident with the temperatures at which the perovskite phase transition occurs (Figure 4A–E) and the low-temperature evolution trend of device performance changes (Figure 2D–G). These floating integrated intensities were therefore correlated to the phase transition of the perovskite, jointly changing the device performance. The corresponding 2D GIWAXS patterns and texture at characteristic temperatures are presented in Figures S11 and S12 (Supporting Information), respectively. These patterns show consistent peak positions without shift as the temperature changes and the close peak intensity. These results indicate that the films have no preferred crystallite orientation, and that the texture is not changing with time.

Even more, we extracted the out-of-plane and in-plane direction GIWAXS patterns by integrating the diffraction area with the azimuth from 89 to 91° and from 0 to 2°, respectively. The coexistence of tetragonal and cubic phases at low temperatures is reflected in Figures S13 and S14 (Supporting Information). However, the cubic-to-tetragonal phase transition temperature is not consistent for these. Under cooling down, the out-of-plane direction has an earlier phase transition temperature happening after −25 °C (Figure S15A, Supporting Information), compared to ≈ −65 °C in plane (Figure S16A, Supporting Information). During the heating process, the perovskite shows a practically identical phase transition termination at −20 °C between out-of-plane and in-plane (Figures S15B and S16B, Supporting Information). This turning point is close to phase transition temperature during the cooling process in the out-of-plane direction, farther than that in the in-plane direction. This result suggests that the perovskite structure is recovered in the out-of-plane direction. Still, the recovery process in the in-plane direction is suppressed. Such perovskite phase transition is also reflected in the linear non-uniformity of scattering vector (Figures S17 and S18, Supporting Information).

2.4. Elucidating Perovskite Structural Transformation Mechanism

Figure 5 displays the temperature evolution of the scattering vector q. Cycling temperatures, the q along the out-of-plane direction evolved from 10.03 to 10.27 nm^{-1}. This was greater than the value ranging from 10.07 to 10.19 nm^{-1} of the in-plane (Figure 5A,B; Figure S19, Supporting Information). The used perovskites have initially the same composition and crystallinity. The shift of the diffraction peaks is mainly caused by temperature variation, relating to the formation of macroscopic strain. We therefore employed the equation $\sigma = [E/q_0(1+\nu)] \cdot \Delta q$ instead of Williamson–Hall method to evaluate lattice strain, where E is Young's modulus evaluated as 10 GPa, ν is Poisson's ratio evaluated as 0.3, and the scattering vector constant q_0 is 10.12 nm^{-1}.[35–37] It can be observed that the lattice strain σ is directly proportional to Δq, which represents the difference between the out-of-plane ($q_\perp$) and in-plane ($q_\parallel$) scattering vector (Table S5, Supporting Information).[38–40] The perovskite film's out-of-plane direction experiences an entirely reversible q value (Figure 5A), indicating that the out-of-plane direction of the film returns to entirely

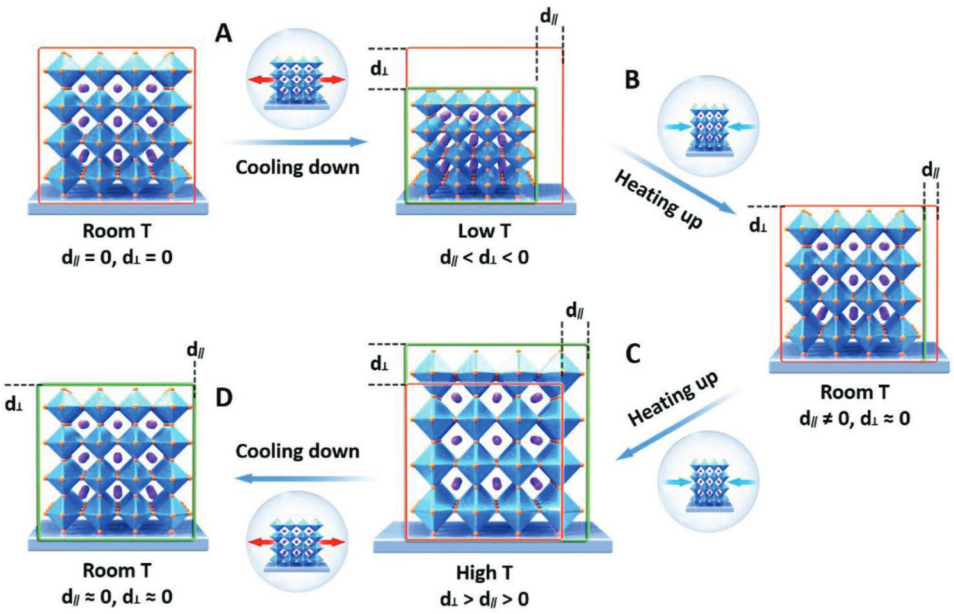

Figure 6. Schematic of the evolution of the perovskite film strain with temperature. Deformation of perovskite film structure during A) cooling down from room temperature, B) heating up to room temperature again, C) further heating, and D) finally cooling down to room temperature. $d_{\perp}$ and $d_{//}$ represent the lattice shrinkage or expansion in the out-of-plane and in-plane directions.

strain-free after temperature cycling. However, the in-plane direction shows a certain degree of hysteresis (Figure 5B), and thus a residual strain after temperature cycling.[16,41–43]

Plotting Δq as a function of the temperature in Figure 5C, we have an overview of the lattice strain as a function of the temperature cycling. Perovskite film experiences an increasing strain as the temperature is lowered below and above room temperature. However, when passing through room temperature, the strain is almost entirely released regardless of the cooling or heating history of the sample.

We summarized the evolution of the perovskite film strain under thermal cycling in **Figure 6**.

I. Cooling from room temperature, the perovskite film experiences an in-plane tensile strain since shrinkage along the in-plane (d_{II}) was smaller than the out-of-plane ($d_{\perp}$) direction ($d_{II} < d_{\perp} < 0$).
II. Heating again to room temperature results in an in-plane compressive strain since the film does not recover the in-plane (d_{II}) completely while it recovers the out-of-plane ($d_{\perp}$) dimensions ($d_{II} < d_{\perp} \approx 0$).
III. Further heating at higher temperatures releases the in-plane compressive strain and induces a tensile strain in the same direction since $d_{\perp} > d_{II} > 0$.
IV. Cooling to room temperature again releases strains ($d_{II} \approx d_{\perp} \approx 0$).

3. Conclusion

This work examined the performance evolution of perovskite solar cells over a broad temperature window from –160 to 150 °C. Reducing the temperature to below –50 °C, the device experiences a considerable PCEs reduction despite a V_{oc} increase. While heating the device, the PCEs decline marginally due to the slight drop in V_{oc}. The PCE trend relates well to the perovskite phase transition and crystal disordering. The tetragonal to cubic phase transition at low-temperature results in an abrupt change in PCE. Besides the phase transitions, the decrease and increase in temperature, respectively, endow an inconsistent cold compression and hot expansion of the perovskite film between out-of-plane and in-plane directions. Returning to room temperature, the crystal structure releases the strain and the PCE recovers systematically. Our work highlights the prospects of perovskite-based PV operating in extreme temperature environments like those experienced in extraterrestrial conditions.

Supporting Information

Supporting Information is available from the Wiley Online Library or from the author.

Acknowledgements

G.L. and Z.S. contributed equally to this work. The authors thank Helmholtz-Zentrum Berlin for funding. The authors acknowledge financial support from the Natural Science Foundation of China (no. 51903181). The authors would also like to acknowledge support from the UK EPSRC ATIP Programme grant (EP/T028513/1) and the EPSRC fund on SPECIFIC Innovation and Knowledge Centre (EP/N020863/1). G.L. acknowledges China Scholarship Council (CSC) for the financial support (grant no. 201906150131). J.J.J., R.R., and M.S. acknowledge the German Research Foundation for funding via the priority program SPP2196. G.L., M.F., and H.K. thank the support from the HyPerCells Joint Graduate

School. The authors thank beamline BL14B1 at the Shanghai Synchrotron Radiation Facility (SSRF) for providing the beam time. This work has received funding from the European Research Council (ERC) under the European Union's Horizon 2020 research and innovation programme (grant agreement no. 804519).

Conflict of Interest

The authors declare no conflict of interest.

Data Availability Statement

Research data are not shared.

Keywords

aerospace, lattice strain, perovskite structures, photovoltaics, thermal stability

Received: August 24, 2022
Revised: October 15, 2022
Published online:

[1] S. G. Yalew, M. T. H. van Vliet, D. E. H. J. Gernaat, F. Ludwig, A. Miara, C. Park, E. Byers, E. De Cian, F. Piontek, G. Iyer, I. Mouratiadou, J. Glynn, M. Hejazi, O. Dessens, P. Rochedo, R. Pietzcker, R. Schaeffer, S. Fujimori, S. Dasgupta, S. Mima, S. R. S. da Silva, V. Chaturvedi, R. Vautard, D. P. van Vuuren, *Nat. Energy* **2020**, *5*, 794.
[2] A. Harjanne, J. M. Korhonen, *Energy Policy* **2019**, *127*, 330.
[3] D. Bogdanov, J. Farfan, K. Sadovskaia, A. Aghahosseini, M. Child, A. Gulagi, A. S. Oyewo, L. de Souza Noel Simas Barbosa, C. Breyer, *Nat. Commun.* **2019**, *10*, 1077.
[4] D. E. H. J. Gernaat, H. S. de Boer, V. Daioglou, S. G. Yalew, C. Müller, D. P. van Vuuren, *Nat. Clim. Change* **2021**, *11*, 119.
[5] A. Kojima, K. Teshima, Y. Shirai, T. Miyasaka, *J. Am. Chem. Soc.* **2009**, *131*, 6050.
[6] Best Research-Cell Efficiency Chart – NREL, https://www.nrel.gov/pv/assets/pdfs/best-research-cell-efficiencies-rev220126.pdf (accessed: June 2022).
[7] L. Chouhan, S. Ghimire, C. Subrahmanyam, T. Miyasaka, V. Biju, *Chem. Soc. Rev.* **2020**, *49*, 2869.
[8] L. K. Reb, M. Böhmer, B. Predeschly, S. Grott, C. L. Weindl, G. I. Ivandekic, R. Guo, C. Dreißigacker, R. Gernhäuser, A. Meyer, P. Müller-Buschbaum, *Joule* **2020**, *4*, 1880.
[9] J. Barbé, A. Pockett, V. Stoichkov, D. Hughes, H. K. H. Lee, M. Carnie, T. Watson, W. C. Tsoi, *J. Mater. Chem. C* **2020**, *8*, 1715.
[10] Y. Tu, J. Wu, G. Xu, X. Yang, R. Cai, Q. Gong, R. Zhu, W. Huang, *Adv. Mater.* **2021**, *33*, 2006545.
[11] Z. Dong, W. Li, H. Wang, X. Jiang, H. Liu, L. Zhu, H. Chen, *Sol. RRL* **2021**, *5*, 2100370.
[12] S. Shao, J. Liu, H.-H. Fang, L. Qiu, G. H. ten Brink, J. C. Hummelen, L. J. A. Koster, M. A. Loi, *Adv. Energy Mater.* **2017**, *7*, 1701305.
[13] A. K. Jena, Y. Numata, M. Ikegami, T. Miyasaka, *J. Mater. Chem. A* **2018**, *6*, 2219.
[14] A. D. Sheikh, R. Munir, M. A. Haque, A. Bera, W. Hu, P. Shaikh, A. Amassian, T. Wu, *ACS Appl. Mater. Interfaces* **2017**, *9*, 35018.
[15] Y. Chen, S. Tan, N. Li, B. Huang, X. Niu, L. Li, M. Sun, Y. Zhang, X. Zhang, C. Zhu, N. Yang, H. Zai, Y. Wu, S. Ma, Y. Bai, Q. Chen, F. Xiao, K. Sun, H. Zhou, *Joule* **2020**, *4*, 1961.
[16] J. Zhao, Y. Deng, H. Wei, X. Zheng, Z. Yu, Y. Shao, E. S. Jeffrey, J. Huang, *Sci. Adv.* **2017**, *3*, eaao5616.
[17] M. Kaltenbrunner, G. Adam, E. D. Głowacki, M. Drack, R. Schwödiauer, L. Leonat, D. H. Apaydin, H. Groiss, M. C. Scharber, M. S. White, N. S. Sariciftci, S. Bauer, *Nat. Mater.* **2015**, *14*, 1032.
[18] F. Lang, M. Jošt, J. Bundesmann, A. Denker, S. Albrecht, G. Landi, H.-C. Neitzert, J. Rappich, N. H. Nickel, *Energy Environ. Sci.* **2019**, *12*, 1634.
[19] A. Ullah, K. H. Park, H. D. Nguyen, Y. Siddique, S. F. A. Shah, H. Tran, S. Park, S. I. Lee, K.-K. Lee, C.-H. Han, K. Kim, S. Ahn, I. Jeong, Y. S. Park, S. Hong, *Adv. Energy Mater.* **2022**, *12*, 2103175.
[20] M. A. Green, *Prog. Photovolt. Res. Appl.* **2012**, *20*, 954.
[21] J. Barbé, D. Hughes, Z. Wei, A. Pockett, H. K. H. Lee, K. C. Heasman, M. J. Carnie, T. M. Watson, W. C. Tsoi, *Sol. RRL* **2019**, *3*, 1900219.
[22] Y. Tu, G. Xu, X. Yang, Y. Zhang, Z. Li, R. Su, D. Luo, W. Yang, Y. Miao, R. Cai, *Sci. China Phys. Mech.* **2019**, https://doi.org/10.1007/s11433-019-9356-1.
[23] C. R. Brown, G. E. Eperon, V. R. Whiteside, I. R. Sellers, *ACS Appl. Energy Mater.* **2019**, *2*, 814.
[24] C. Xu, X. Chen, S. Ma, M. Shi, S. Zhang, Z. Xiong, W. Fan, H. Si, H. Wu, Z. Zhang, Q. Liao, W. Yin, Z. Kang, Y. Zhang, *Adv. Mater.* **2022**, *34*, 2109998.
[25] H. X. Dang, K. Wang, M. Ghasemi, M.-C. Tang, M. D. Bastiani, E. Aydin, E. Dauzon, D. Barrit, J. Peng, D.-M. Smilgies, S. D. Wolf, A. Amassian, *Joule* **2019**, *3*, 1746.
[26] H. Tan, F. Che, M. Wei, Y. Zhao, M. I. Saidaminov, P. Todorović, D. Broberg, G. Walters, F. Tan, T. Zhuang, B. Sun, Z. Liang, H. Yuan, E. Fron, J. Kim, Z. Yang, O. Voznyy, M. Asta, E. H. Sargent, *Nat. Commun.* **2018**, *9*, 3100.
[27] S. Wu, J. Zhang, Z. Li, D. Liu, M. Qin, S. H. Cheung, X. Lu, D. Lei, S. K. So, Z. Zhu, A. K.-Y. Jen, *Joule* **2020**, *4*, 1248.
[28] W. Peng, X. Miao, V. Adinolfi, E. Alarousu, O. El Tall, A.-H. Emwas, C. Zhao, G. Walters, J. Liu, O. Ouellette, J. Pan, B. Murali, E. H. Sargent, O. F. Mohammed, O. M. Bakr, *Angew. Chem., Int. Ed.* **2016**, *55*, 10686.
[29] T. Baikie, Y. Fang, J. M. Kadro, M. Schreyer, F. Wei, S. G. Mhaisalkar, M. Graetzel, T. J. White, *J. Mater. Chem. A* **2013**, *1*, 5628.
[30] C. Barone, F. Lang, C. Mauro, G. Landi, J. Rappich, N. H. Nickel, B. Rech, S. Pagano, H. C. Neitzert, *Sci. Rep.* **2016**, *6*, 34675.
[31] C. Xu, Z. Zhang, S. Zhang, H. Si, S. Ma, W. Fan, Z. Xiong, Q. Liao, A. Sattar, Z. Kang, Y. Zhang, *Adv. Funct. Mater.* **2021**, *31*, 2009425.
[32] G. Li, Z. Su, M. Li, F. Yang, M. H. Aldamasy, J. Pascual, F. Yang, H. Liu, W. Zuo, D. Di Girolamo, Z. Iqbal, G. Nasti, A. Dallmann, X. Gao, Z. Wang, M. Saliba, A. Abate, *Adv. Energy Mater.* **2021**, *11*, 2101539.
[33] M. Qin, K. Tse, T. K. Lau, Y. Li, C.-J. Su, G. Yang, J. Chen, J. Zhu, U.-S. Jeng, G. Li, H. Chen, X. Lu, *Adv. Mater.* **2019**, *31*, 1901284.
[34] B. J. Kim, G. Boschloo, *Nanoscale* **2021**, *13*, 11478.
[35] N. Rolston, K. A. Bush, A. D. Printz, A. Gold-Parker, Y. Ding, M. F. Toney, M. D. McGehee, R. H. Dauskardt, *Adv. Energy Mater.* **2018**, *8*, 1802139.
[36] J. Yu, M. Wang, S. Lin, *ACS Nano* **2016**, *10*, 11044.
[37] M. A. Reyes-Martinez, A. L. Abdelhady, M. I. Saidaminov, D. Y. Chung, O. M. Bakr, M. G. Kanatzidis, W. O. Soboyejo, Y.-L. Loo, *Adv. Mater.* **2017**, *29*, 1606556.
[38] H. Wang, C. Zhu, L. Liu, S. Ma, P. Liu, J. Wu, C. Shi, Q. Du, Y. Hao, S. Xiang, H. Chen, P. Chen, Y. Bai, H. Zhou, Y. Li, Q. Chen, *Adv. Mater.* **2019**, *31*, 1904408.
[39] C. Zhu, X. Niu, Y. Fu, N. Li, C. Hu, Y. Chen, X. He, G. Na, P. Liu, H. Zai, Y. Ge, Y. Lu, X. Ke, Y. Bai, S. Yang, P. Chen, Y. Li, M. Sui, L. Zhang, H. Zhou, Q. Chen, *Nat. Commun.* **2019**, *10*, 815.
[40] G. Jian, Y. Jiao, Q. Meng, Y. Guo, F. Wang, J. Zhang, C. Wang, K.-S. Moon, C.-P. Wong, *Nano Energy* **2021**, *82*, 105778.
[41] R. Cheacharoen, N. Rolston, D. Harwood, K. A. Bush, R. H. Dauskardt, M. D. McGehee, *Energy Environ. Sci.* **2018**, *11*, 144.
[42] H.-S. Kim, N.-G. Park, *NPG Asia Mater.* **2020**, *12*, 78.
[43] Y. Jiao, S. Yi, H. Wang, B. Li, W. Hao, L. Pan, Y. Shi, X. Li, P. Liu, H. Zhang, C. Gao, J. Zhao, J. Lu, *Adv. Funct. Mater.* **2021**, *31*, 2006243.